scientific reports

OPEN

Plasticity-based design and static performance of UT-type joint for construction error adaptation

Sun Menghan, He Luyao, Jiang Xin, Yang Zailin✉ & Yang Miaomiao

To solve the problem of insufficient development of prefabricated rectangular hollow section (RHS) beam-column joints, a new type of prefabricated joint (UT-type joint) is proposed in this paper. The problem of construction error is effectively solved using a unique structural design, and the plastic energy dissipation section is introduced based on the concept of plastic controllability. This research mainly includes three aspects: (1) a new type of beam-column loading test device is designed, and a static loading test of the UT-type joint is carried out to evaluate the static performance of the joint; (2) through finite element simulation, the static performances of UT-type joints and traditional RHS joints are compared; and (3) based on the existing specifications and simulation results, a simplified design method for UT-type joints is proposed. The main research findings are as follows: (1) the static bearing capacity of the UT-type joint is slightly lower than that of the traditional RHS joint, with a maximum decrease of 15.4%; and (2) compared with the traditional RHS joint, the UT-type joints exhibit better plastic controllability, lower axial force sensitivity, and construction error adjustment ability (± 5 mm adjustment by adjusting the sleeve). These advantages give UT-type nodes a good application prospect.

In line with China's development strategy, the Ministry of Housing and urban–rural development has set a high-quality development framework for the prefabricated building sector in its 14th five-year plan. This framework includes promoting the upgrading of intelligent construction and production, expanding the application of standardized components, and improving the overall efficiency of prefabricated building[1,2].

In the development of prefabricated building, beam-column joints have always been a research focus, and scholars in China and abroad have made important contributions to the research and development of new prefabricated beam-column joints. For example, Li Yuanqi et al. proposed a beam-column hinged joint with replaceable energy dissipation elements and obtained key parameters such as the strength, stiffness, ductility, and hysteretic curves of the joint[3,4]. Tong Lewei designed three types of joints with different connection structures and studied the hysteretic behavior of truss joints under cyclic axial force[5–12]. The cyclic loading test showed that the welding part between the brace and the gusset plate is the weak point and that it is prone to cracking[13]. Yang Junping et al. proposed a new type of steel structure assembly joint. The plastic deformation of this new joint is transferred from the core area of the joint to the outside, which meets the seismic requirements of strong joint and weak member. The bearing capacity of the joint is improved by increasing the thickness of the end plate[14,15].

Regarding these studies, we noted that there has been relatively limited development of fabricated beam-column joints for rectangular hollow section (RHS) beam structures[16,17]. RHS beams, a commonly used structural element, offer high bending and torsional stiffness, and they have been widely applied in construction[18–21]. To promote the development of a prefabricated rectangular tube structure system, the technical code for a green prefabricated rectangular tube structure system has been approved by the China Building Materials Market Association. The code is mainly focused on the development of new prefabricated beam-column joints.

Previous research on prefabricated steel beam-column joints has mainly focused on the reliability and energy dissipation capacity of the joints, but it has ignored the practical problem of construction error[22–25]. As a result, some new prefabricated beam-column joints are difficult to install in practical applications.

In response to the aforementioned issues and learn from previous experiences[26–30], this paper innovatively proposes a novel prefabricated joint, namely, the UT-type joint. This joint effectively addresses the problem of installation errors during construction through adjustment of the sleeves. In addition, the design concept of a dog-bone joint is used as a reference, and an energy dissipation section is added at the beam-column connection.

Harbin Engineering University, Harbin, Heilongjiang, China. ✉email: 194008496@qq.com
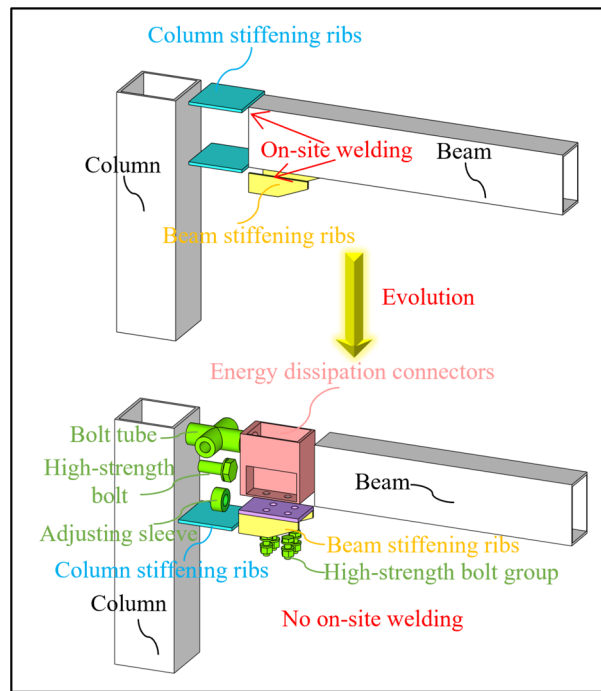
**Fig. 1**. Structural diagram of UT-type fabricated joint.
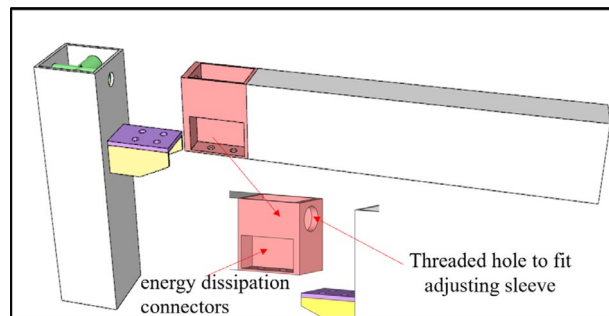
Fig. 2. Installation process 1.

By reducing the bending capacity of the connection section, the plastic hinge is formed in the energy dissipation section before the high-strength bolt bears a large amount of stress, which significantly improves the energy dissipation performance of the joint. Compared with the traditional RHS joint, UT-type joints exhibit better plastic controllability, lower axial force sensitivity, and construction error adjustment ability.

Joint construction and assembly method

The UT-joints are shown in Fig. 1 and include beams, columns, adjusting sleeves, and energy dissipation connectors. This new type of prefabricated joint is developed on the basis of the traditional square steel tube beam-column structure. The all-bolt connection is realized by preinstalling the connecting member on the column. The problem of construction error is solved by adjusting the close fit between the sleeve and column flange. In addition, the joint incorporates an energy dissipation segment between the beam and the column (source of the UT-joint's name, where the cross-section corresponds to the letters UT). By reducing the bending capacity of the energy dissipation connection section, the plastic hinge is formed before the high-strength bolt produces a large amount of stress, which greatly improves the energy dissipation capacity of the new joint.

Factory prefabricated units are hoisted to designated elevations (Fig. 2). During the factory prefabrication stage, the bolt tubes and beam stiffening ribs are welded to the RHS columns, and holes are made at the corresponding positions, with the center of each hole aligned with the bolt tube. Simultaneously, the energy dissipation connectors are welded to the ends of the RHS beams, and a threaded hole for the adjusting sleeves (Fig. 8) is reserved in the front end plate, ensuring that the center of the hole is aligned with the center of the bolt tube. This ensures the proper axial alignment of the entire set of components during field installation.
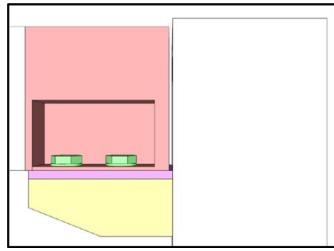
Fig. 3. Installation process 2.
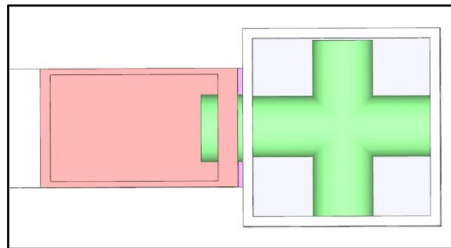
Fig. 4. Installation process 3.
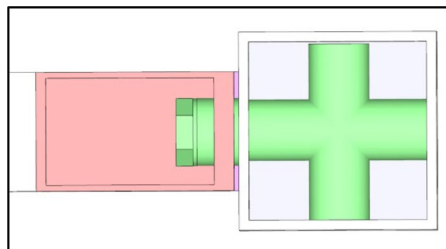
Fig. 5. Installation process 4.

The high-strength bolt group was installed at the lower part of the joint (Fig. 3). We note that there is a certain distance deviation between the energy-dissipating segment and the column due to the construction error.

The adjusting sleeve is screwed into the energy dissipation joint area and attached to the column wall (the outer surface of the adjusting sleeve has threads matching the energy dissipation joint area) to adjust the construction error (Fig. 4).

The upper high-strength bolt is connected (Fig. 5). High-strength bolt connections should be tightened using a torque wrench. The torque wrench can be extended into a groove at the top of the energy dissipation connectors to apply the pre-tightening force to the high-strength bolt, with the preset torque value specified in the design requirements, ensuring that the bolt's pre-tightening force meets the specified standards.

Designs of experiment and simulation of UT-joint
Design of experimental equipment and loading scheme
The static loading test method was employed to investigate the failure modes, load-bearing capacity, and plastic rotation capability of the prefabricated UT-type joints. First, in accordance with the Specification for Seismic Testing Methods of Buildings[31], a novel beam-column loading experimental apparatus was designed. The test setup is illustrated in Fig. 6.

It should be noted that the test setup employs a beam base instead of connection columns (Fig. 6). The rationale for this design is based on the strong column and weak beam principle, where the failure of the prefabricated UT-type joints is concentrated at the energy-dissipating connection ends, while the columns do not exhibit significant damage. Therefore, the focus of the test was primarily on the failure of the energy-dissipating connection ends and the high-strength bolt groups. Simplifying the column structure to a beam base does not affect the test results, and it reduces the cost of the experiment.

In the static loading test, the specimen was first subjected to pre-loading treatment, with two cycles of pre-loading, and repeated load tests were conducted. The applied load in each cycle did not exceed 10% of the plastic limit moment of the joint. The loading protocol strictly adhered to the relevant regulations of the quasi-static loading test. Due to the high initial stiffness of the joint during the initial loading phase, force control was first
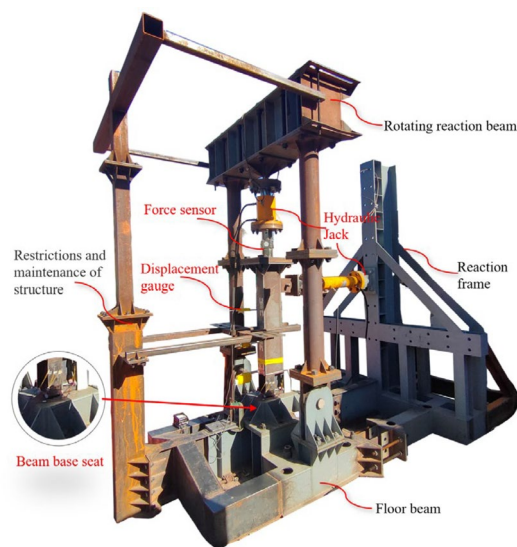
Fig. 6. Diagram of the experimental equipment on-site.

Joint number	i(μ)	Loading condition	Loading direction
UT-1	0	No axial force	Obverse
UT-2	0	No axial force	Reverse
UT-(i)ZL-1	0.4	Axial Tension	Obverse
UT-(i)ZL-2	0.4	Axial Tension	Reverse
UT-(i)ZY-1	0.4	Axial Compression	Obverse
UT-(i)ZY-2	0.4	Axial Compression	Reverse

Table 1. Joint number and corresponding working condition.

employed for loading. Before reaching the ultimate moment, the loading was divided into 50 stages. In each successive stage, the load was increased by 0.5 kN·m, and the holding time for each stage was approximately 3 min. After reaching the ultimate moment, displacement control was used to conduct the loading, which was divided into 10 stages. In each subsequent stage, the jack displacement was increased by 4 mm, and the holding time for each stage was approximately 5 min. Data collection was performed after the joint deformation stabilized in each loading stage.

To systematically study the influence of the axial force on the static behavior of the prefabricated UT-type joints, four groups of static tests were designed. The specific working conditions and joint numbers are shown in Table 1. The specific size of the specimen is shown in Fig. 5. To simplify the expression, a new index called the axial force ratio (μ) is introduced, which is defined as the ratio of the absolute value of the joint axial force to the product of the full cross-sectional area (A_g) and the design value of the steel tensile strength (f_y) (Fig. 7). The calculation formula is as Eq. (1):

$$\mu = \frac{|N|}{A_g f_y}. \tag{1}$$

The bolt group and adjustment sleeve used in the UT-type prefabricated joint are shown in Fig. 8, and the construction error between the beam specimen and the beam base is illustrated in Fig. 9. The quasi-static loading test primarily focused on the energy dissipation segment of the prefabricated UT-type joint. Strain gauges were arranged to monitor the stress variations during the loading process, thereby assessing the plastic development of the energy dissipation segment. Figure 10 shows the arrangement of the strain gauge for the prefabricated UT-type joint.

Material properties test
The energy dissipation connections in the test specimens were made of Q235 steel with thickness of either 2.7 mm or 3.7 mm, depending on the specimen design. Uniaxial tensile tests were conducted on these two types of steel in accordance with the relevant regulations[32]. The material property test specimens are shown in Fig. 11.

The constitutive relationships of the various steels were measured as shown in Figs. 12 and 13. The upper yield strength (R_{eH}) was defined as follows: the first peak stress (the first maximum stress) before yielding is taken as the upper yield strength, regardless of whether the subsequent peak stresses are larger or smaller than it.
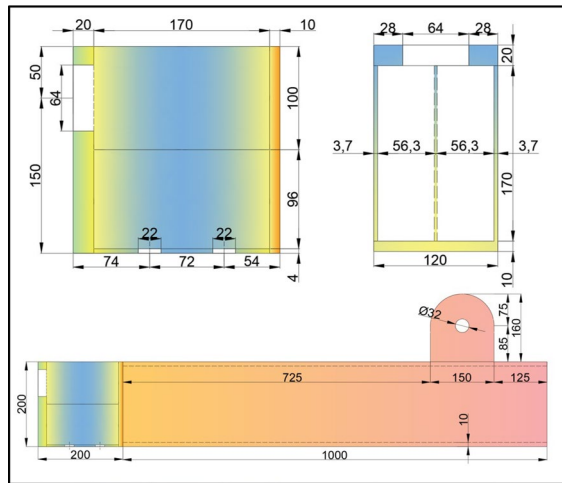
Fig. 7. Test specimen dimensions.

Fig. 8. Fasteners for specimen.
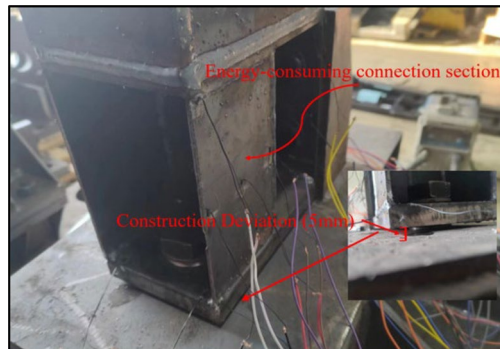
Fig. 9. Photograph showing the installed specimen.

The average R_{eH} value measured for each group was taken as the upper yield strength for each material. The final measured R_{eH} value of the 3.7-mm-thick Q235 steel was 263.5 MPa, and that of the 2.7-mm-thick Q235 steel was 308.2 MPa. Similarly, the lower yield strength was defined as the stress R_{eL} corresponding to the minimum force in the yield stage, excluding the initial transient effect. The measured R_{eL} value for the 3.7-mm-thick Q235 steel was 268.28 MPa, and that of the 2.7-mm-thick Q235 steel was 315.4 MPa. The ultimate stress was taken as the tensile strength R_m, which represents the maximum stress value achieved after material strengthening. The measured R_m values of the 3.7-mm-thick Q235 steel and 2.7-mm-thick Q235 steel were 421.09 MPa and 433 MPa, respectively. The characteristic values of the two materials are presented in Table 2.

To enhance the simulation computation speed, the material property test data obtained from the experiments were simplified using the commonly employed trilinear model for steel[33]. The stress–strain values of the lower yield point R_{eL} and the ultimate stress Rm were taken as the inflection points of the curve. For the 3.7-mm-thick Q235 steel, R_{eL} was taken as 263.5 MPa, corresponding to a strain of 0.0013; and R_m was taken as 421.09 MPa,
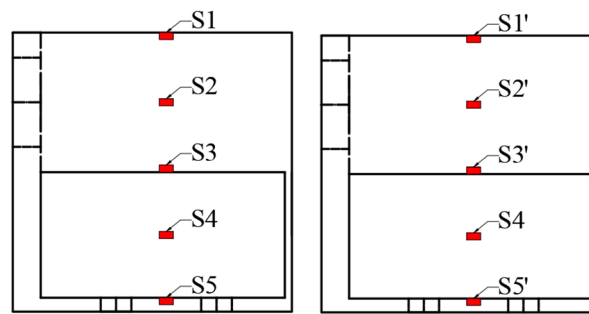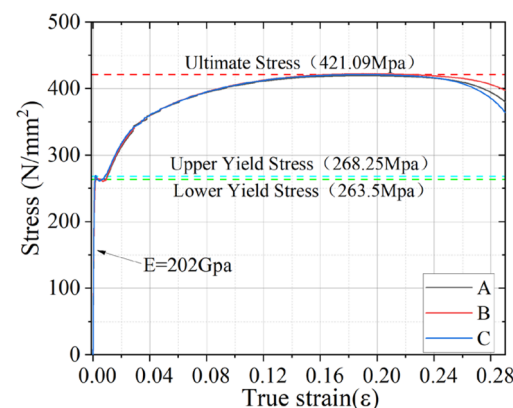
Fig. 10. Locations of strain gauges.

(a) Before the experiment (b) After the experiment

Fig. 11. Material property test specimens. (**a**) Before the experiment. (**b**) After the experiment.

Fig. 12. True stress–strain of steel (3.7 mm).

corresponding to a strain of 0.197. Similarly, for the 2.7-mm-thick Q235 steel, R_{eL} was 308.2 MPa, with a corresponding strain of 0.0014; and R_m was taken as 433 MPa, with a strain of 0.1948.

Establishment of numerical simulation model

To further investigate the mechanical performance of the prefabricated UT-type joints and conduct parameter analysis, it was necessary to establish corresponding numerical simulation models. In this study, we employed the ABAQUS software to analyze the joints, and the model dimensions were consistent with the dimensions of the experimental specimens (Fig. 20). The joint components were simulated as solid elements (C3D8R), and the joint model meshes were all structured meshes. To prevent stiffness distortion in the calculation process of single-layer mesh integration, which would lead to premature local buckling failure of the joint, the thickness direction was divided into at least three layers of structural meshes during the meshing process. To enhance the computational speed of the model while preserving the stress information of the critical sections, such as the energy-consuming connections, local mesh refinement was applied to the model. The resulting mesh division is illustrated in Fig. 14.

During the loading process, the column ends were hinged, and the connection positions between the gasket and the bolt, as well as between the gasket and the base plate, were consistent with actual engineering
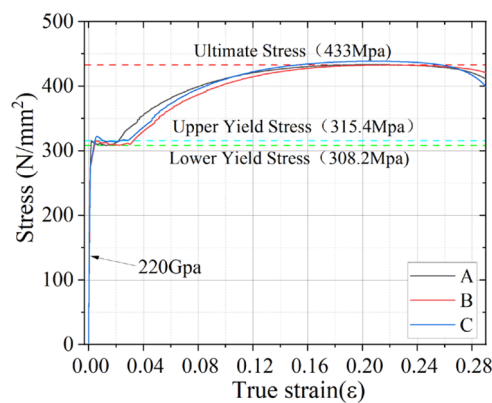
Fig. 13. True stress–strain of steel (2.7 mm).

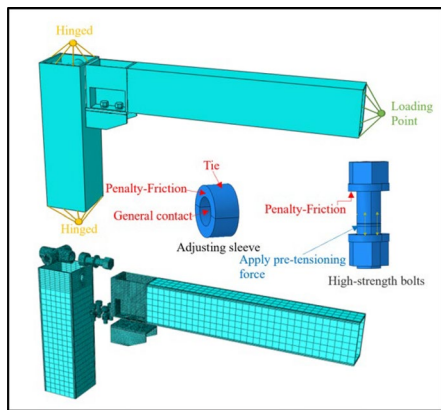| Type of steel	E (GPa)	R_m (MPa)	R_{eH} (MPa)	R_{eL} (MPa)	δ(%)
3.7 mm Q235	202	421.09	268.25	263.5	21.6%
2.7 mm Q235	220	433	315.4	308.2	58.5%

Table 2. Mechanical properties of steel materials.

**Fig. 14**. Finite element model of the UT-type joint.

practices. The penalty-friction contact method was uniformly adopted, with a friction coefficient of 0.3. Due to the significant computational resources required for simulating thread engagement, the tie contact was used to model the threaded connection, and it was also applied to the outer side of the adjustment sleeve. Similar to the gasket, since the inner diameter of the adjustment sleeve was larger than the diameter of the screw, there was no contact behavior between them until the screw underwent substantial deformation. Therefore, the general contact method was employed to simulate this mechanical behavior.

The numerical calculation model was segmented according to the plate thickness, and different material parameters were assigned to various positions. The material properties of the energy-dissipating connection segments were consistent with the simplified trilinear model derived from the experimental data. For the steel plates with thicknesses that were not measured in the tests, the material parameters adhered to the relevant requirements specified in the Code for *the* Design of Steel Structures[34]. This code simplifies the stress–strain relationship curve of Q235 steel as a bilinear model, with a yield stress of 235 MPa, an ultimate stress of 370 MPa, an elastic modulus of 200 GPa, and a post-yield hardening elastic modulus set to 0.01 times the initial elastic modulus[35–37].

The model was established based on the specific geometric parameters and material properties outlined in the standards for High-Strength Large Hexagon Nuts for Steel Structures and High-Strength Bolts for Steel Structures[38,39]. According to the relevant provisions, the yield strength of the high-strength bolt material in the finite element model was $f_y = 940$ N/mm^2, and the ultimate tensile strength was $f_u = 1040$ N/mm^2. Preloading forces were applied to the high-strength bolts in accordance with the actual engineering requirements, with preloading forces of 327.6 kN for the M30 high-strength bolts and 142.7 kN for the M20 high-strength bolts[35].
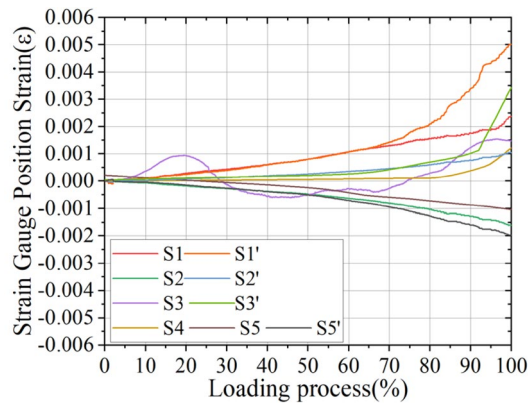
Fig. 15. Strain curve of the UT-type joint under positive moment loading.
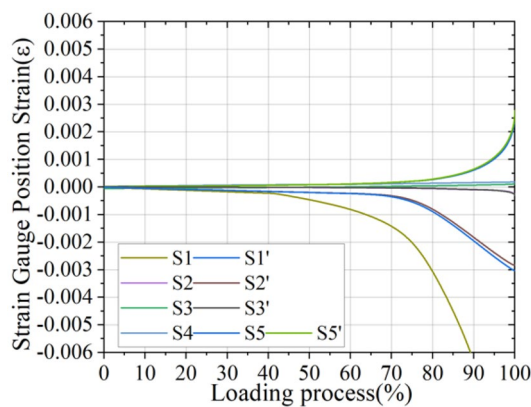
Fig. 16. Strain curve of the UT-type joint under negative moment loading.

The loading conditions of the model were consistent with the tests, that is, the axial force was applied first, and then, bending moment loading was applied in the subsequent analysis steps.

Static loading test of UT-type node
### Experimental phenomena
The failure mode of the UT-type assembled joint under positive bending moment is illustrated in Fig. 24. It can be observed that the joint zone experienced significant deflection, with a θ value reaching 0.04 rad. Due to the constraint of the high-strength bolts, the energy-dissipating joint zone in region B underwent local buckling under compression. In region A, which was subjected to tension, the energy-dissipating joint zone exhibited obvious tensile yield failure. The failure mode of the joint was consistent with the results of the finite element simulation. During the loading process (Fig. 15), when the drift angle reached 0.02 rad, the strains at the positions of strain gauges S1 and S1' exceeded the yield strain. At a drift angle of 0.028 rad, the strain at the position of strain gauge S2 surpassed the yield strain. When the drift angle reached 0.04 rad, the strains at the positions of strain gauges S5', S3', and S4 all exceeded the yield strain, indicating the formation of a plastic hinge in the energy dissipation node region. By measuring the distance between the front end plate and the beam base, it was found that the high-strength bolts did not undergo significant deformation, that is, the distance remained consistent with the pre-loading measurement at 5 mm. This confirms that the high-strength bolts in the upper part did not fail during the node failure.

The failure mode under the negative bending moment is illustrated in Fig. 25. It was found that the upper side plate of the energy dissipation joint zone experienced inward buckling failure (Area A). Area B exhibited yielding failure due to tension, while the high-strength bolt group at the bottom did not exhibit any slippage. At this point, the rotation angle θ of the joint zone was 0.05 rad. In the finite element simulation results, outward buckling failure occurred in the energy dissipation joint zone. The primary reason for the discrepancy in the failure modes lies in the deviation of the upper side plate of the energy dissipation joint zone during the manufacturing process. The strain distribution is shown in Fig. 16. The strain at location S1 exceeded the yield strain when loaded to 0.02 rad, and at 0.035 rad, the energy dissipation node zone's yielding position extended to regions S2 and S2'. The S5 region surpassed 2000 $\varphi\varepsilon$ when loaded to 0.05 rad, resulting in full-section yielding of
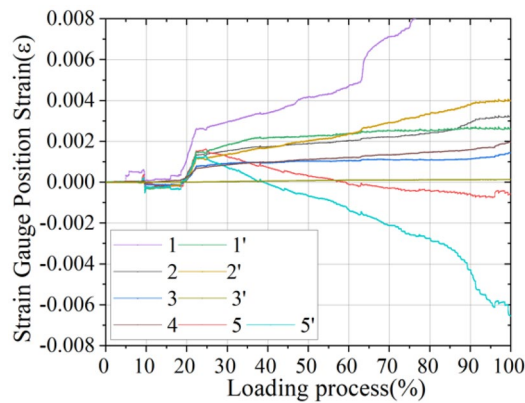
Fig. 17. Strain curve of the UT joint under axial tension and positive moment coupling loading (0.4μ).
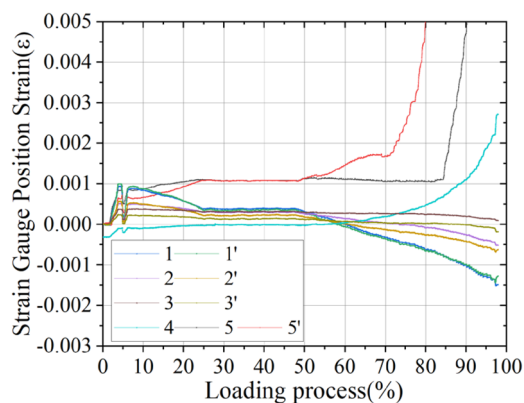
Fig. 18. Strain curve of the UT joint under axial tension and negative moment coupling loading (0.4μ).

the energy dissipation node zone. Throughout the loading process, the gap between the front end plate and the beam base remained at 5 mm, and no significant changes were observed.

The failure mode of the joint under the coupling effect of 0.4μ axial tension and the positive bending moment is illustrated in Fig. 26. Compared to pure bending loading, the distinguishing feature of this failure mode is that at the same rotation angle, the coupling effect of the tension and bending prevented significant warping deformation at the bottom of the energy dissipation segment. Due to the axial tension, the initial stiffness of the joint increased by 42.63% compared to that under pure bending loading, while its yield moment decreased notably by approximately 6.35%. By analyzing the strain data (Fig. 17), it was found that after applying 0.4μ axial tension, the strain values of each strain gauge approached 1000 με. The material property tests revealed that the yield strain of this steel was about 2000 με, further confirming the accuracy of the applied axial tension. As the positive bending moment was applied, the strain values of strain gauges 1 and 1' in the upper part of the energy dissipation segment rapidly increased, and the yield strain was reached at a rotation angle of approximately 0.005 rad (corresponding to region A in Fig. 26). Subsequently, at a rotation angle of around 0.01 rad, the strain at strain gauges 2 and 2' successively exceeded 2000 με and entered the yield stage, while strain gauge 5' experienced a compressive strain greater than – 2000 με. At the final node failure, at the position of strain gauge 4, the strain remained tensile strain, clearly indicating that under axial tension, the neutral axis of the node shifted toward the bottom of the energy dissipation segment. The strain variations during the loading process aligned with the simulation results. The measurements indicate that after the node failure, the gap between the front end plate and the column flange remained approximately 5 mm, and the high-strength bolts at the top did not fail. The high-strength bolt group in the lower part of the energy dissipation zone did not exhibit any slippage.

The failure mode of the joint under the coupling effect of 0.4μ axial tension and negative bending moment is shown in Fig. 27. Compared to pure bending loading, the distinguishing feature of this failure mode is that under the same rotation angle, the coupling of the tension and bending caused significant warping deformation at the bottom of the energy dissipation segment (area B). At the time of failure, the warping value was approximately 5 mm, and a slight slippage phenomenon occurred in the high-strength bolt group in the lower part of the energy dissipation section. The axial tensile force restricted the buckling deformation of the top connecting plate in the energy dissipation segment, resulting in a 21.18% increase in the initial stiffness of the joint compared to pure bending loading, while the ultimate bending moment decreased by approximately 1.21%. By analyzing the strain data (Fig. 18), it was found that after applying a 0.4μ axial tensile force, the initial strain values of all of the strain

gauges were close to 1000 με. As the loading progressed, the strain values recorded by strain gauges 5 and 5' rapidly increased due to the warping force, entering the yielding stage. Subsequently, the strain value recorded by strain gauge 4 exceeded 2000 με near a rotation angle of 0.16 rad, indicating that the lower region of the energy dissipation segment had entered the plastic stage. Due to the axial pressure, the upper part of its energy-dissipating connection end exhibited significant instability failure (area A in Fig. 27). At the time of failure, the strains at strain gauges 1, 1', 2, 2', 3, and 3' did not exceed 2000 με. As shown by the stress cloud diagram in Fig. 27, the stress on the upper connecting plate did not reach the yield stress at the time of node failure.

The failure mode of the prefabricated UT-type joint under the combined action of 0.4μ axial compression and the positive bending moment is illustrated in Fig. 28. Compared to pure bending loading, the joint deformation at yield failure was smaller, which can also be observed in the joint moment-rotation curve (Fig. 22). Under the combined action of 0.4μ axial compression and the positive bending moment, the joint entered the yield stage at a rotation angle of 0.006 rad, which was significantly less than the yield rotation at 0.0012 rad under pure bending loading. From the failure photographs of the joint, it can be seen that the warping at the edge of the front plate was not severe under the coupled axial compression, and the high-strength bolts remained intact. Compared to pure bending loading, the initial stiffness of the joint increased by approximately 11.7% under the coupled effect of the axial pressure and positive bending moment, while the yield moment value decreased significantly, by about 24.5%. Through analysis of the strain data (Fig. 19), it was found that after the loading was completed, the strain values of sections 1, 1', 2, and 2' in the upper energy dissipation segment all exceeded 2000 με, indicating tensile yielding; while those in sections 3', 4, 5, and 5' exceeded −2000 με, indicating compressive yielding. Additionally, sections 2 and 2' experienced abrupt changes at a rotation angle of approximately 0.015 rad; sections 5' and 3' also experienced sudden strain changes, and the strain in section 4' ceased to increase. This phenomenon occurred due to buckling failure in the upper connecting plate of the energy dissipation segment, which caused an instantaneous increase in the joint rotation angle. At this point, the neutral axis of the joint approached the location of the strain gauge in section 4' (corresponding to the stress contour in Fig. 33), resulting in cessation of the strain increase in section 4'. Consequently, the energy dissipation segment developed a full cross-section, forming a plastic hinge.

The failure mode of the UT-type prefabricated joint under the combined action of 0.4μ axial pressure and the negative bending moment is illustrated in Fig. 29. Under this loading condition, the upper connecting plate of the energy dissipation segment experienced instability failure when the joint rotation reached 0.001 rad, leading to a sudden decrease in the joint stiffness of approximately 16.16%. Compared to pure bending loading, the yield bending moment decreased by about 9.2%. According to the strain curve (Fig. 20), during the loading process, the strains at strain gauges 1 and 1' exceeded 2000 με at a rotation angle of approximately 0.01 rad, and those at strain gauges 2 and 2' exceeded 2000 με at a rotation angle of about 0.015 rad. Upon completion of the loading, it was observed that the positions of strain gauges 3 and 3' experienced compressive yielding, while the position of strain gauge 5' did not exhibit tensile yielding, and the neutral axis of the joint shifted significantly downward (corresponding to the stress cloud diagram in Fig. 29). Based on the failure characteristics, it was also found that after loading, the upper region of the energy dissipation segment underwent buckling failure (Area A in Fig. 29), while the lower region of the energy dissipation segment did not exhibit significant failure characteristics.

According to the load and resistance factor design (LRDF) specification, the yield moment of the joint under the combined action of the axial force and bending moment was calculated. The calculation process is shown in Fig. 21. The calculation results are presented in Table 3. It can be observed that the yield moment values of the joint calculated based on the LRDF specification are conservative under axial tension. Under axial compression, due to manufacturing errors in the energy dissipation segment, the upper connecting plate experienced earlier buckling failure (Fig. 29), resulting in theoretical yield moment values higher than those measured in the tests. Additionally, it should be noted that the yield moment values obtained from the numerical simulations are generally slightly higher than those measured in the tests. The overall error remains at around 10%, which is within the acceptable error range.

According to the values in Table 3, it was found that under axial tension, the K_y value of the UT-0.4ZL-1 group increased by approximately 42.6% compared to that of UT-1; under negative bending moment loading, its
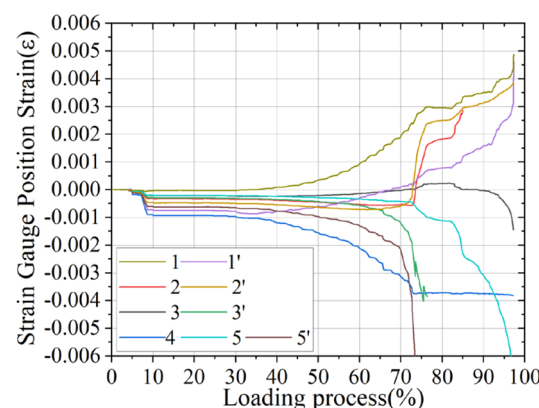
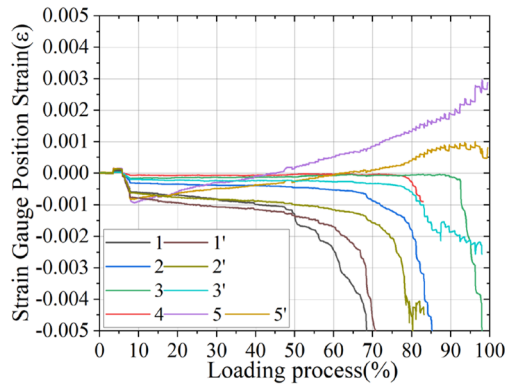**Fig. 19**. Strain curve of the UT joint under axial compression and positive moment coupling loading (0.4μ).

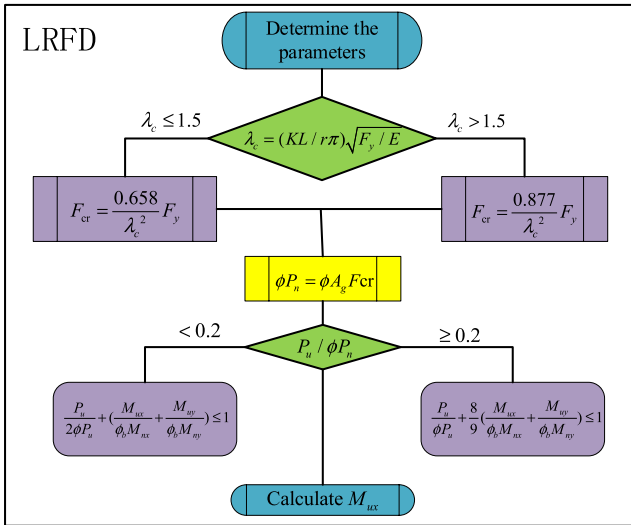**Fig. 20.** Strain curve of the UT joint under axial compression and negative moment coupling loading (0.4μ).


Fig. 21. Theoretical calculation process.

Joint ID	K_y (kN·m/rad) Experimental data	K_y (kN·m/rad) Simulated data	M_y (kN·m) Experimental data	M_y (kN·m) Simulated data	M_y (kN·m) Theoretical value
UT-1	4440.16	4019.29 9.4% ↓°	25.1	27.5 8.7% ↑•	27.07(308 MPa) 7.3% ↑*
UT-2	3879.31	3757.53 3.1% ↓°	20.0	20.87 4.3% ↑•	21.7(263 MPa) 8.2% ↑*
UT-0.4ZL-1	6333.33	6882.59 8.7% ↑°	23.6	21.8 8.2% ↓•	22.8(308 MPa) 3.5% ↓*
UT-0.4ZL-2	4700.85	4938.18 4.8% ↑°	19.76	17.95 9.1% ↓•	19.5(263 MPa) 1.3% ↓*
UT-0.4ZY-1	4,959.88	4,157.48 16.2% ↓°	18.94	17.56 7.8% ↓•	22.4(308 MPa) 15.4% ↑*
UT-0.4ZY-2	3,252.48	2711.32 19.9% ↓°	18.16	16.91 6.8% ↓•	19.2(263 MPa) 5.4% ↑*

Table 3. Characteristic values of joint force performance. Asterisk (*): Experimental vs. theoretical yield moment. Bullet (•): Numerical vs. experimental yield moment. Circle (°): Numerical vs. experimental initial stiffness.

K_y value increased by about 21.1%. Under axial compression, the change in the K_y value of the joint was relatively small, with differences of 11.7% and 16.1% compared to pure bending loading, respectively. Additionally, it should be noted that under axial compression, the difference between the numerically simulated K_y value and the experimental value is the largest (18.1%). The reason for this phenomenon may be that under axial
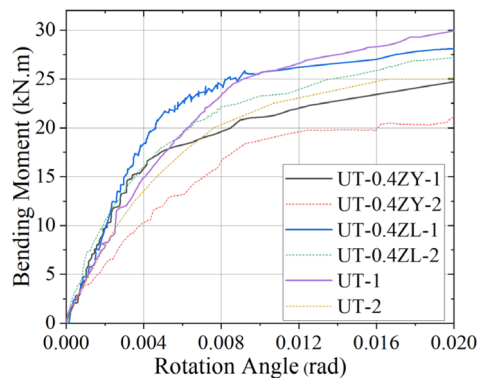
Fig. 22. Moment-rotation curve of UT-type joint (experimental data).
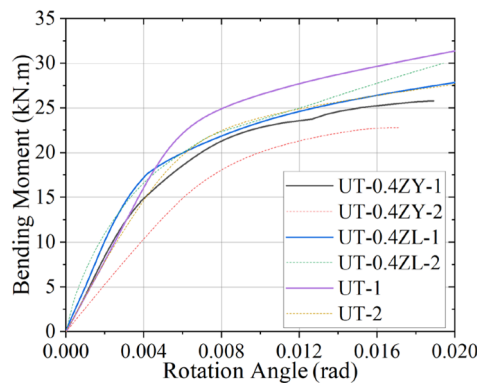
Fig. 23. Moment-rotation curve of UT-type joint (simulation data).

compression, the contact gap between the external threads of the adjusting sleeve and the threads of the front end plate increased, reducing the ability of the two to work in coordination, thereby leading to a significant difference between the K_y value and the simulation results.

Test results

The calculation results of the LRDF procedure indicate the load-bearing performance of the consolidated joints. Through comparison of the experimental and theoretical calculation results, it was found that the load-bearing performance of the UT-type prefabricated joints was slightly lower than that of the consolidated joints, and the yield moment value was up to 15.4% lower. However, this new type of joint is a fully bolted prefabricated joint, and its installation efficiency is significantly better compared to those of the consolidated joints. Therefore, the prefabricated UT-type joint has promising application prospects.

According to the data for the initial stiffness K_y, it was found that the K_y value of this new type of joint is not significantly affected by axial force. Additionally, it was found that under most loading conditions, the energy dissipation section of the new joint experienced full-section yield failure, which aligns with the design concept of controllable plasticity. This demonstrates that the prefabricated UT-type joint possesses excellent energy dissipation capabilities.

By comparing the moment-rotation curves in Figs. 22 and 23, the simulation curves and experimental curves exhibit consistent trends, and the errors of the initial stiffness K_y and yield moment M_u are within approximately 10%, which is within an acceptable range. The largest discrepancy occurs under the 0.4 axial compression negative moment loading condition, under which the initial stiffness K_y difference is 19.9%. This phenomenon may be attributed to the use of tie contact instead of threaded connections. Additionally, it should be noted that as the axial force increased, the rotation at node failure decreased in both the simulation and experimental results. In summary, the fitting results for each group of nodes are satisfactory, further validating the accuracy of the numerical model and laying a foundation for subsequent parameter analysis of the numerical model (Figs. 24, 25, 26, 27, 28 and 29)[40].

### Static load simulation of UT-type joint
Design of specimen

To compare the mechanical performance differences between the fabricated UT-type joints and existing steel beam-column joints, three RHS beam–column joints were designed according to the corresponding
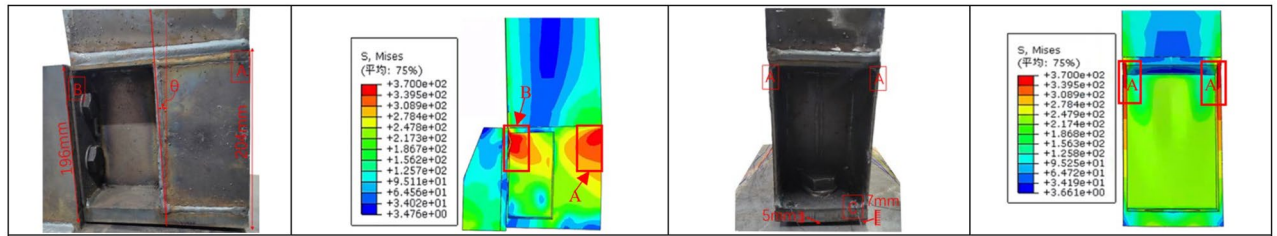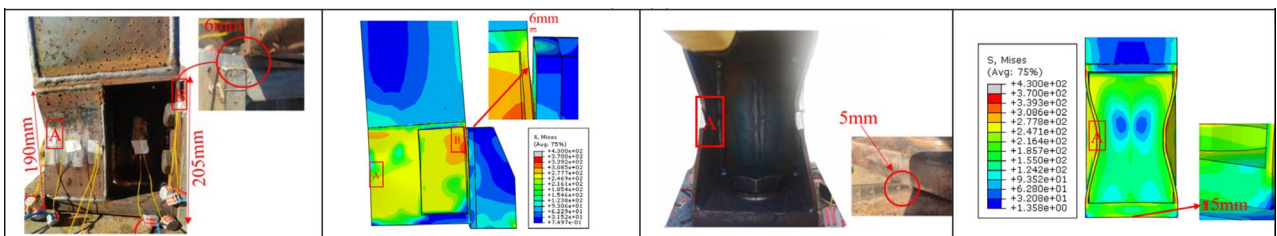
Fig. 24. Failure diagram for the UT-type joint under positive moment loading.
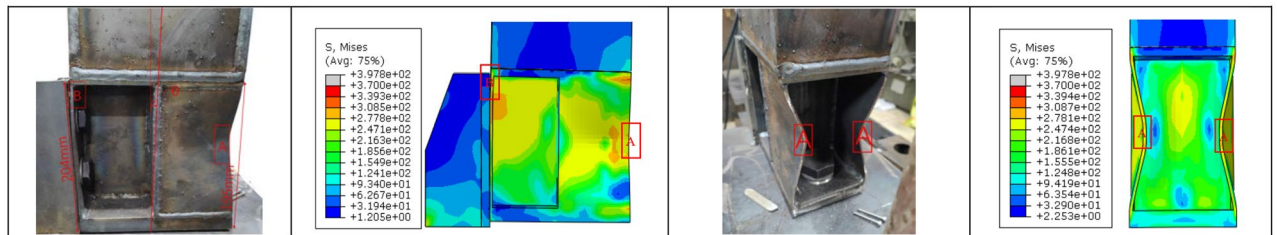
Fig. 25. Failure diagram for the UT-type joint under negative moment loading.
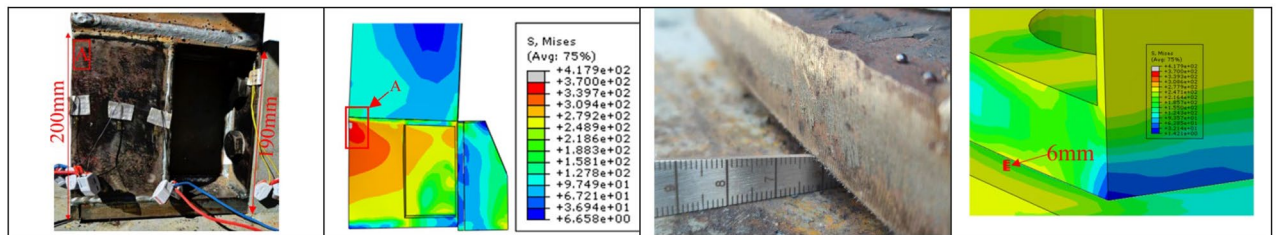
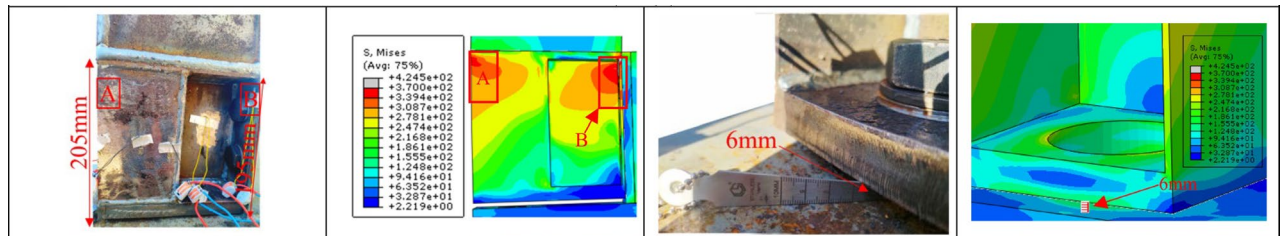Fig. 26. Failure diagram for the UT-type joint under axial tension and positive moment coupling loading (0.4μ).

Fig. 27. Failure diagram for the UT-type joint under axial tension and negative moment coupling loading (0.4μ).

specifications and construction experience(The bolted-welded joint is SH-RHS (120×200) and the bolted joint is S-RHS (120×200))[41]. Dimensions of each joint can be found in Figs. 30, 31 and 32. The materials used for each joint are listed in Table 4. The parameters of the Q235 material are consistent with those of the steel structure design specification adopted above, and the parameters of the 40Cr material are also consistent with those mentioned earlier.

The diameters of the high-strength bolts involved at each node include M36, M20, and M16, and the applied preloads are presented in Table 5.

When meshing the numerical model, we ensured consistency with the previous model by applying mesh refinement to the key components of the numerical model, and we divided the mesh into at least three layers of mesh in the thickness direction.
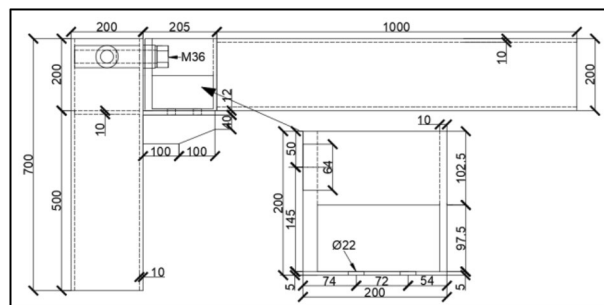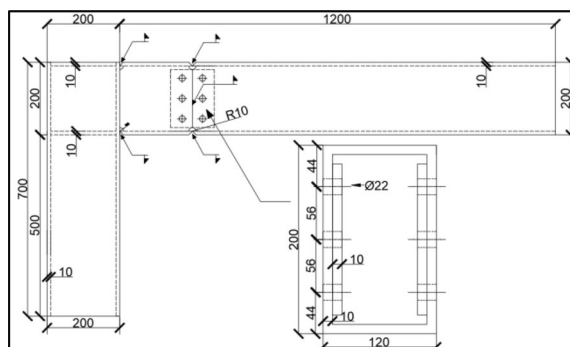
Fig. 28. Failure diagram for the UT-type joint under axial compression and positive moment coupling loading (0.4μ).
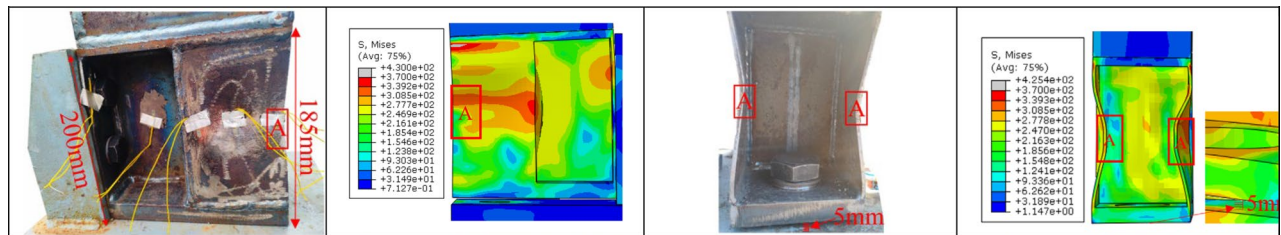
Fig. 29. Failure diagram for the UT-type joint under axial compression and negative moment coupling loading (0.4μ).
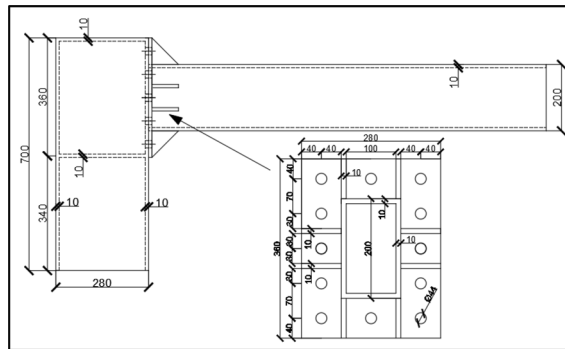

Fig. 30. Diagram showing the dimensions of the assembled UT-type joint.

Fig. 31. Diagram showing the dimensions of the SH-RHS (120×200) joint.

The boundary conditions of the model were also set with hinged connections at both ends of the column, ensuring that the contact conditions in the model matched those in the actual engineering project. A friction coefficient of 0.3 was uniformly applied, and a tie contact was used to simulate the threaded engagement connection. The final mesh division of each node is illustrated in Figs. 33, 34 and 35. The loading pattern was consistent with the aforementioned experimental simulation loading pattern.

Fig. 32. Diagram showing the dimensions of the S-RHS (120×200) joint.

| Joint name	Q235	40Cr
UT-type joint	Beam; Column; Energy-dissipating segment; Bottom plate; Stiffening rib	Bolt cylinder; Adjusting sleeve; High-strength bolt gasket; Nut
SH-RHS (120×200)	Column; Beam; Stiffening rib; Junction plate	High-strength bolt; Gasket; Nut
S-RHS (120×200)	Column; Beam; Stiffening rib; Beam base	High-strength bolt; Gasket; Nut

Table 4. Material list of each joint.

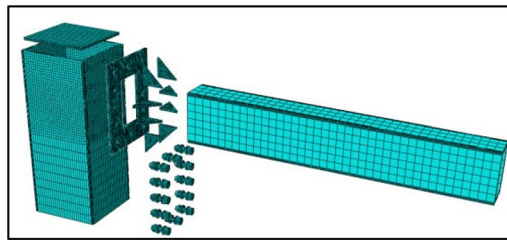| Bolt type	Pre-tightening force (kN)
M36	502
M20	142.7
M16	100

Table 5. Pre-tightening forces of the high-strength bolts.
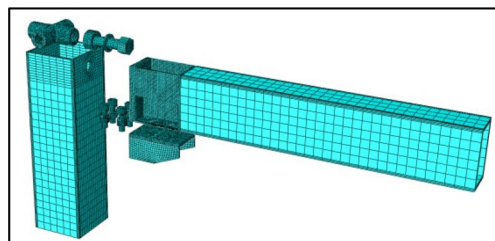
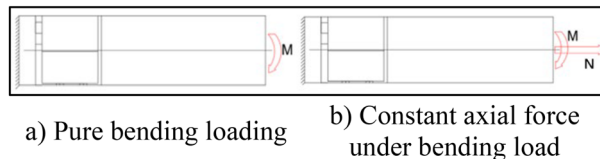**Fig. 33**. Mesh generation of finite element model of UT beam-column joints.
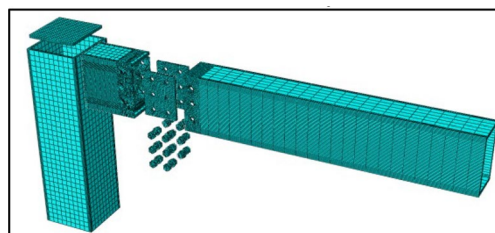
Fig. 34. Mesh generation of finite element model of SH-RHS (120×200) beam-column joints.

Fig. 35. Mesh generation of finite element model of S-RHS (120 × 200) beam-column joints.

a) Pure bending loading   b) Constant axial force under bending load

Fig. 36. Joint loading conditions. (**a**) Pure bending loading. (**b**) Constant axial force under bending load.

Two quasi-static loading conditions were designed according to the actual working conditions (Fig. 36). Because the energy-dissipating segment of the fabricated UT-type joints was asymmetric vertically, to study the mechanical performances of the joints more comprehensively, positive and negative bending moment loading modes were applied to the joints during the bending study.

Simulation calculation results

The bending moment versus rotation angle curves for the three types of beam-column joints under pure bending are shown in Fig. 37. Because the friction between the energy-dissipating segment and the bottom plate contributed to the moment-bearing capacity of the joint, the yield bending moment-bearing capacity of the joint was about 13.18% different when the moment was loaded in two directions. The initial stiffness K_y of the joint was calculated using the elastic ultimate moment value of the joint, and it was concluded that the K_y difference of the joint under the two working conditions was about 11.9% (Table 6). The UT-type node locally weakened the energy dissipation connection segment. Therefore, by comparing the moment-rotation curves of the different nodes, it was found that under pure bending conditions, the initial stiffness K_y of the fabricated UT-type joint was 57.3% lower than that of the S-RHS (120 × 200) joint and 44.1% lower than that of the S-RHS (120 × 200) joint. However, it should be noted that the stiffness degradation of the prefabricated UT-type joint was relatively gradual, with a decrease of approximately 37.27% in the joint stiffness K_y at the yield moment, while the other two types of joints exhibited decreases of 43.2% (SH-RHS (120 × 200)) and 40% (S-RHS (120 × 200)). Figures 38, 39 and 40 present the stress nephograms of each member when the final joint was destroyed. In Fig. 38, it can be seen that under the action of the ultimate bending moment, the entire section of the UT-type energy dissipation joint yielded, while the beam section only yielded at the maximum local stress, and the high-strength bolt group, bottom plate, and stiffening rib were not destroyed. As shown in Figs. 39 and 40, the SH-RHS (120 × 200) joint was destroyed due to the full-section yield at the edge of the joint domain. The S-RHS (120 × 200) joint was damaged due to buckling at the base of the beam.

The bending moment and rotation curves of the three types of beam-column joints under constant-tension and bending loads are shown in Fig. 41, and the elastic–plastic ultimate bending moment and initial stiffness data are presented in Table 7. It can be observed that unlike the UT-type joint, the mechanical characteristics of the other two types of joints are significantly influenced by axial tension. At an axial compression ratio of 0.5μ, the yield moment M_y of the SH-RHS (120 × 200) joint decreased by approximately 80.1%, while that of the S-RHS (120 × 200) joint decreased by about 66%. In contrast, the prefabricated UT-type joint experienced a reduction in M_y of approximately 63.5% under positive moment loading and of 66% under negative moment loading. The initial stiffness K_y values further highlight the minimal impact of the axial tension on the UT-type joint. At an axial compression ratio of 0.5μ, the initial stiffness K_y of the UT-type joint only decreased by 7.7%, whereas the other two types of joints exhibited reductions of approximately 83.03% and 86.4%.

As can be seen from the moment-rotation curves in Fig. 41a,b, under constant tension bending conditions, the ultimate moment value and initial stiffness of the UT-type joint decrease relatively slowly. The underlying mechanism of this phenomenon can be attributed to the internal force redistribution within the energy-dissipating connection segment under axial tension. The position of the neutral axis exhibited significant variations in response to axial forces of different magnitudes. Notably, even in the failure stage, the energy-dissipating connection segment maintained full-section yielding characteristics. The stress distribution patterns are illustrated in Figs. 42 and 43, which present the stress nephograms of the components of the fabricated UT-type joint under an absolute axial compression ratio value of 0.3. The formation of plastic hinges within the energy-dissipation joint domain can be clearly observed in these figures. The ultimate bending moments of the S-RHS (120 × 200) and SH-RHS (120 × 200) joints decreased rapidly as the absolute value of the axial pressure
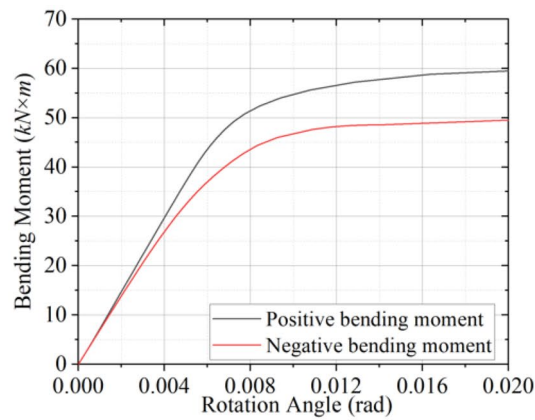
a)   Prefabricated UT-type joint
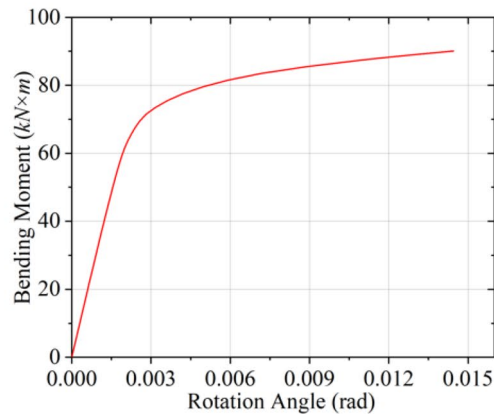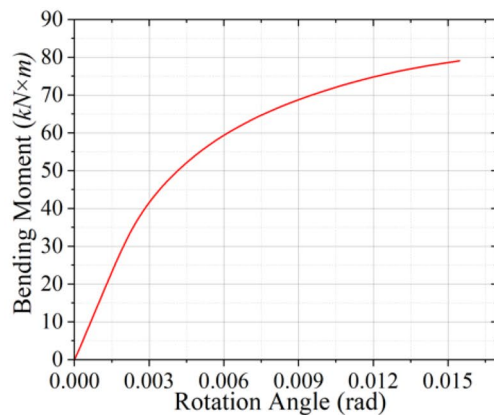
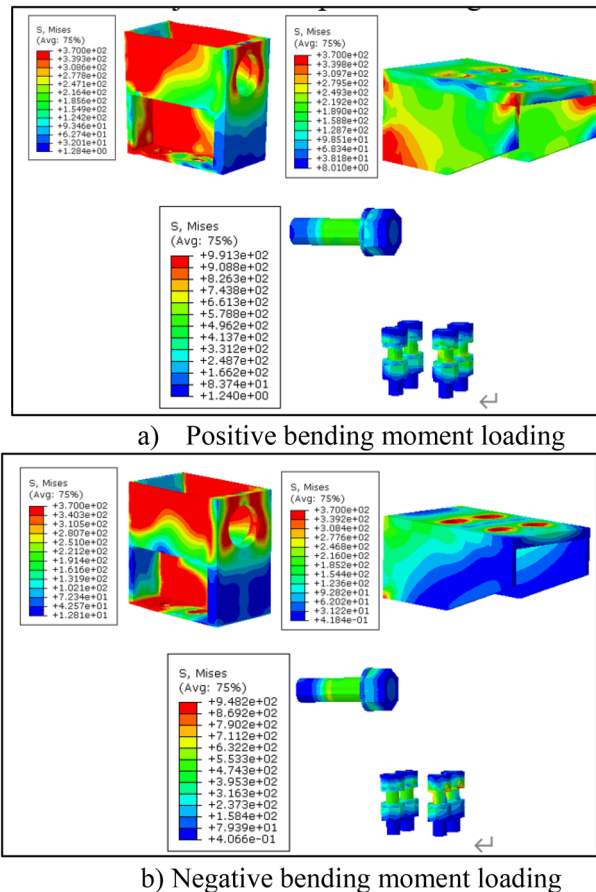b) S-RHS (120 × 200) joint

c) S-RHS (120 × 200) joint

Fig. 37. Bending moment versus rotation angle of each beam-column joint under pure bending loading. (**a**) Prefabricated UT-type joint. (**b**) S-RHS (120×200) joint. (**c**) S-RHS (120×200) joint.

increased. The cause of this phenomenon can be observed from the stress contour map. Figures 44 and 45 show the stress nephograms of each member under the conditions of constant tension and bending when the absolute value of the axial compression ratio was 0.3. The failure modes of the aforementioned two types of nodes were characterized by local yielding, and this phenomenon became more pronounced under axial tension; thus, their mechanical performance was more significantly influenced by the axial tensile forces.

The bending moment and rotation curves of the three types of beam-column joints under constant-pressure and bending loads are shown in Fig. 46, and the limited bending moment value and initial stiffness data are presented in Table 8. Similar to axial tension and bending, the yield moment M_y and initial stiffness K_y of the UT-type joints were less affected by the axial force. At an axial compression ratio of 0.5μ, the M_y value decreased by approximately 48.7%, and the K_y value decreased by approximately 12.5%. For the SH-RHS (120×200)

| Joint name	M_y	M_u	K_y
Assembled UT-type joint	36.4	60.4	7413
Assembled UT-type joint	31.6	49.5	6529
SH-RHS (120×200) joint	49	92	17,379
S-RHS (120×200)	32	79	13,264

Table 6. Yield loads and initial stiffnesses of joints under pure bending loads.

a) Positive bending moment loading

b) Negative bending moment loading

Fig. 38. Stress nephogram for UT joint under pure bending loading. (**a**) Positive bending moment loading. (**b**) Negative bending moment loading.
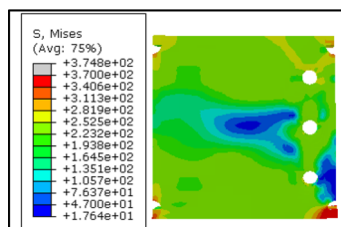
Fig. 39. Stress nephogram for SH-RHS (120×200) pure bending loaded member.

joints, the M_y value decreased by approximately 85.5%, and the K_y value decreased by approximately 90.2%. For the S-RHS (120×200) joints, the M_y value decreased by approximately 86.3%, and the K_y value decreased by approximately 91.8%.

As can be seen from Fig. 46b, under the combined action of axial compression and the negative bending moment, the rotational capacity of the UT-type joint significantly decreased at failure. The reason for this
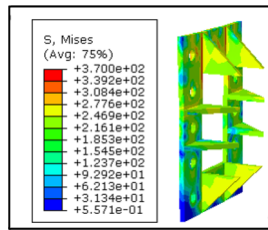
Fig. 40. Stress nephogram for S-RHS (120×200) pure bending loaded member.

phenomenon lies in the fact that under this loading condition, the upper connecting side plate at the energy-dissipating end is subjected to the compressive stress resulting from the superposition of the axial pressure and negative bending moment, causing it to enter the yielding stage earlier and thereby reducing the joint's deformation capacity. This can also be seen in the stress contour plot in Fig. 48, in which only the upper side plate of the energy-dissipating segment exhibits yielding failure at the time of joint failure, and full-section yielding failure does not occur.

Figures 47 and 48 present the stress nephograms of each member of the fabricated UT-type joints subjected to bending failure under constant pressure when the absolute axial compression ratio was 0.3. It can be seen that under positive bending moment loading failure, the energy-dissipating connection end experienced full-section yield failure, and thus, its stress characteristics were less influenced by the axial pressure. However, under negative bending moment loading, due to the coupled effect of the bending moment and axial pressure, the upper side plate of the energy-dissipating connection segment prematurely buckled and failed, resulting in the greater influence of the axial pressure. As indicated by the initial stiffness K_y value, compared to an axial compression ratio of 0.1μ, the K_y value decreased by 9.5% under positive bending moment loading with an axial compression ratio of 0.5μ, while it decreased by 23.3% under negative bending moment loading. Figures 49 and 50 present the stress nephograms of two types of joints, namely, SH-RHS (120×200) and S-RHS (120×200). When the absolute value of the axial compression ratio was 0.3, SH-RHS (120×200) still failed due to local yielding.

Design process of UT-type joint size
To facilitate the practical application of UT-type joints, this paper presents the design process for UT-type joints based on the design principles of the Chinese steel structure design code.

First, the sizes of the beam members are determined. The maximum bearing capacity of the RHS beam in the elastic stage is as follows:

$$M_{LE\,\max} = \frac{\sigma_{\max}I_{LEz}}{y_{LE\,\max}}, \tag{2}$$

where $\sigma_{\max}$ is the design value of the compressive strength of the steel, $M_{LE\,\max}$ is the maximum bending moment of the box beam in the elastic stage, I_{LEz} is the moment of inertia of the beam in the elastic stage around the short-axis direction, and $y_{LE\,\max}$ is the distance from the edge of the beam to the neutral axis in the elastic stage.

The dimensions of the energy-dissipating segment are selected. The dimensions of the outer periphery of the energy dissipation joint domain should be consistent with those of the box beam. To realize plasticity controllability, we suggest that the maximum bearing capacity of the energy dissipation joint domain in the plastic stage be $M_{jU\,\max} = 0.85\,M_{LE\,\max}$. In addition, it is necessary to ensure that the neutral axis in the plastic stage of the joint is located near the X-axis (Fig. 51). Thus, the dimension shown in Fig. 51 should satisfy the following equation:

$$\sigma_{\max}t_1h_1^2 \approx \frac{\sigma_{\max}t_2h_2^2}{2} + \frac{\sigma_{\max}t_3L(h_2+t_3/2)}{2}. \tag{3}$$

The thickness of the front-end version of the energy-dissipating segment is selected. The thickness of the front end plate of the energy-dissipating segment is denoted as t, and the dimensions of the other members remained unchanged. Joint models of the front end plate with thicknesses of 10–28 mm were designed and loaded via pure bending (Figs. 52 and 53). The thickness of the front end plate was 10–20 mm, and the ultimate bending moment of the assembled UT-type joint increased significantly as the thickness of the front end plate increased. For thicknesses greater than 20 mm, the ultimate bending moment value remained basically unchanged. Therefore, when the other components are designed according to Fig. 6, the thickness of the front end plate should be 20 mm. When the other components change, we recommend that the thickness of the front end panel be adjusted to 3.4·t_1.

The high-strength bolts at the bottom are designed. It is required that lower bolt slip failure does not occur in the energy dissipation joint area during loading. The following inequality should be satisfied:
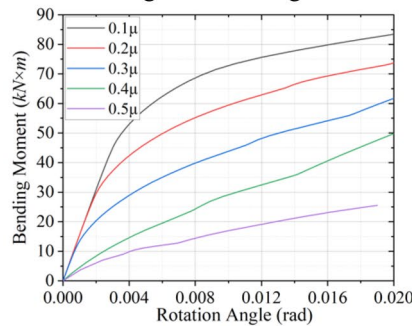
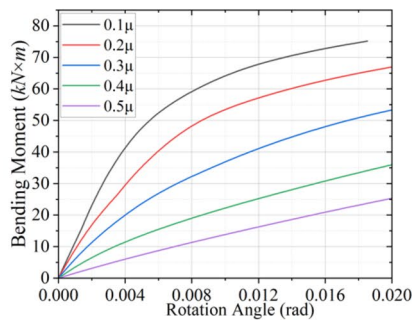$$\mu n N_L \geq 1.1t_3L\sigma_{\max}, \tag{4}$$
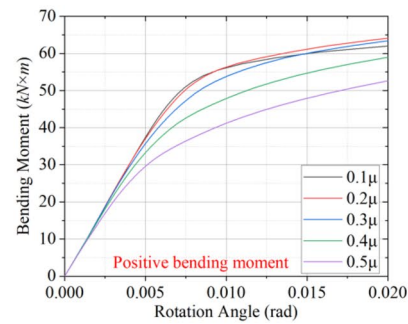
a) UT-type joints subjected to constant tension and positive bending
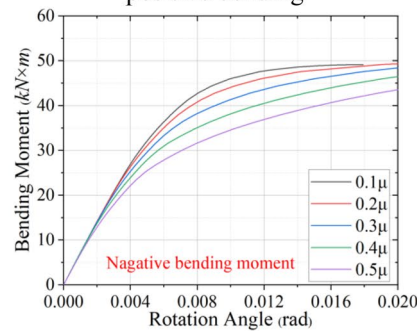
b) UT-type joints subjected to constant tension and negative bending

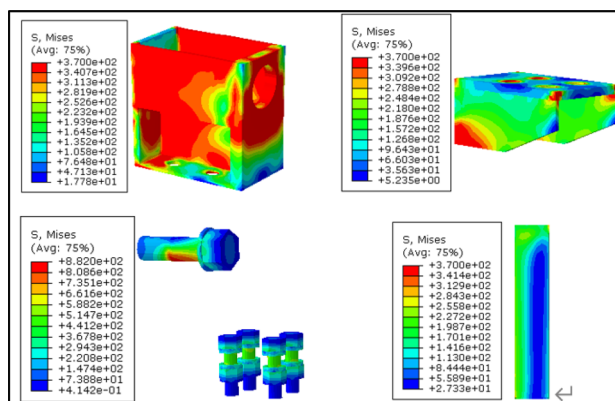c) SH-RHS (120 × 200) under constant tension and bending
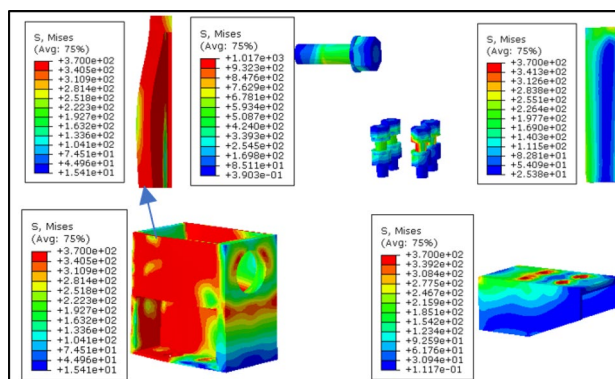

d) S-RHS (120 × 200) under constant tension and bending

Fig. 41. Beam-column joints subjected to constant tension and bending. (**a**) UT-type joints subjected to constant tension and positive bending. (**b**) UT-type joints subjected to constant tension and negative bending. (**c**) SH-RHS (120×200) under constant tension and bending. (**d**) S-RHS (120×200) under constant tension and bending.

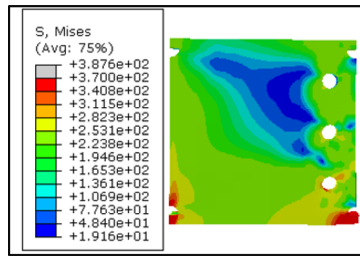| Joint name	Axial compression ratio	M_y	M_u	K_y
UT positive bending moment	0.1 μ	42.8	65.2	7379
	0.2 μ	36.4	63.6	7428
	0.3 μ	30	62	7353
	0.4 μ	20.4	60.4	7208
	0.5 μ	15.6	24.8	6812
UT negative bending moment	0.1 μ	34.8	49.6	6214
	0.2 μ	31.6	49.2	6171
	0.3 μ	28.4	48.2	6055
	0.4 μ	23.6	46	6020
	0.5 μ	18.8	44.4	5875
SH-RHS (120 × 200)	0.1 μ	47.5	83.8	14,600
	0.2 μ	39.5	76.1	11,583
	0.3 μ	28.4	63.6	7357
	0.4 μ	19.8	52.4	3235
	0.5 μ	9.46	25.5	2469
S-RHS (120 × 200)	0.1 μ	47.1	75.2	9600
	0.2 μ	40.1	70.0	7232
	0.3 μ	32.0	62.6	4384
	0.4 μ	20.2	53.0	2448
	0.5 μ	16.0	42.6	1302

Table 7. Yield loads and initial stiffnesses of joints under constant tension and bending loading.
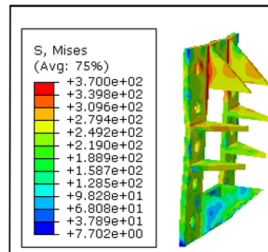

Fig. 42. UT joints with an axial compression ratio of 0.3 subjected to constant tension and positive bending.

Fig. 43. UT joints with an axial compression ratio of 0.3 subjected to constant tension and negative bending.

Fig. 44. SH-RHS (120 × 200) joint with an axial compression ratio of 0.3 under constant tension and bending.

Fig. 45. S-RHS (120 × 200) joint with an axial compression ratio of 0.3 under constant tension and bending.

where μ is the friction coefficient between the bolt and steel, n is the number of bolts in the lower part of the assembled UT-type joints, and N_L is the pre-tightening force of the lower high-strength bolt.

The top high-strength bolts are designed. According to the principle of having a strong joint and a weak member, that is, the upper high-strength bolt should not be damaged before the joint domain under the axial tension condition, we suggest that the following equation be satisfied:

$$N_U \geq 1.2 \cdot (2t_1 h_1 \sigma_{\max} + h_2 t_2 \sigma_{\max} + t_3 L \sigma_{\max} - \mu n N_L) \tag{5}$$

where N_U is the pre-tightening force of the lower high-strength bolt. Finally, the bolt size is selected according to the bolt pre-tightening force.

Conclusions

In this study, we developed a prefabricated UT-type beam-column joint and designed a novel experimental loading device. Through experimental loading, theoretical calculations, and simulation analysis, the following conclusions were obtained.

1. During the failure of the prefabricated UT-type joint, the energy-dissipating connecting section experiences full-section yield failure, while the high-strength bolt group and beam stiffeners remain intact, aligning with the design philosophy of controllable plasticity.

2. Through theoretical calculations, the mechanical performance of the prefabricated UT-type joints is slightly inferior to that of monolithic joints, and the yield moment value is up to 15.4% lower.

3. Simulation studies have revealed that compared to other RHS beam-column joints already used in practical applications, the mechanical performance of prefabricated UT-type joints is less affected by the axial force. However, when the axial compression ratio is relatively large, the rotational capacity of UT-type joints under negative bending moment loading is weaker.

4. Based on the Code for *the* Design of Steel Structures and finite element simulations, the size parameters of the joints were analyzed, and a simplified design method for UT-type joints was proposed, providing theoretical guidance for subsequent engineering design.

In this study, we investigated the static performance of UT-type joints and found that their load-bearing capacity is slightly lower than that of rigid joints. However, as fully bolted prefabricated joints, their installation efficiency is significantly improved compared to those of rigid joints. Additionally, due to the presence of energy-dissipating segments, this new type of joint is expected to have excellent energy dissipation capabilities. Consequently, these joints hold promising application prospects. In the future, we plan to conduct subsequent pseudo-static loading tests to systematically study the energy dissipation capacity of these joints, thereby evaluating the seismic performance of structures utilizing this type of joint.
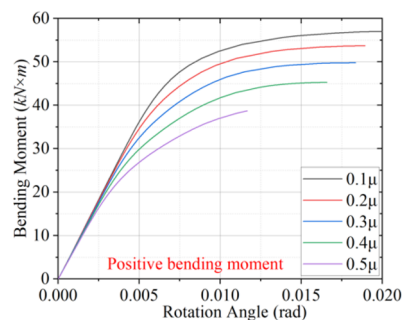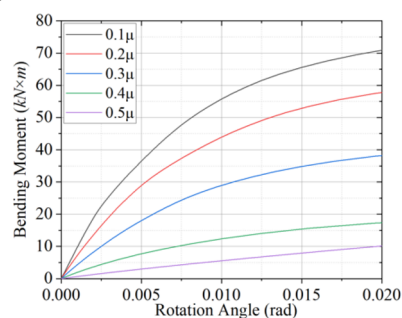
a) UT-type joints subjected to constant pressure and positive bending
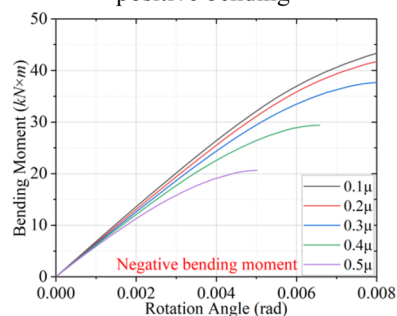
b) UT-type joints subjected to constant pressure and negative bending
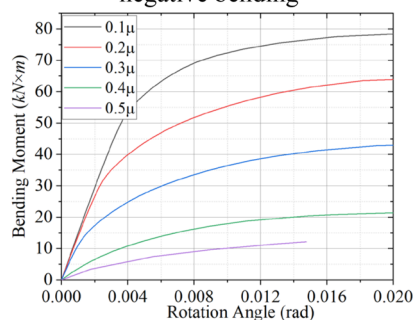
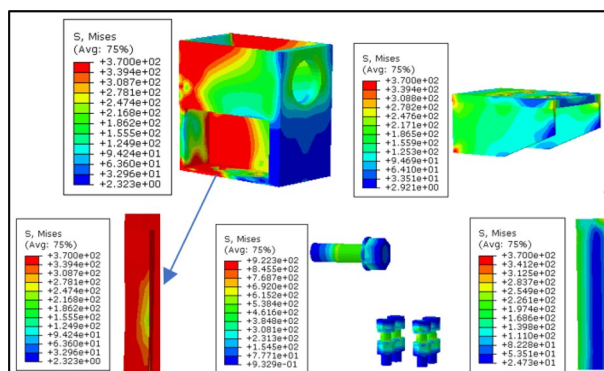c) SH-RHS (120 × 200) bending under constant pressure

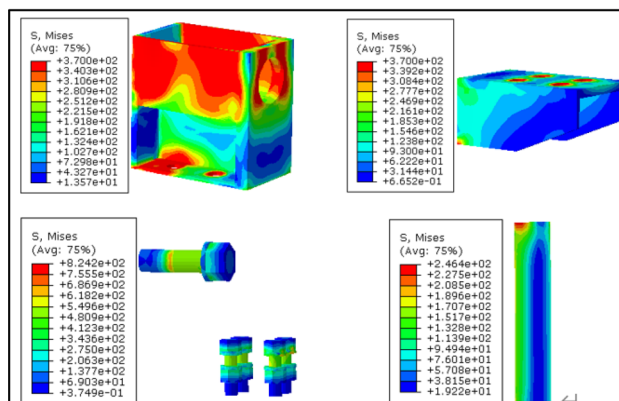d) S-RHS (120 × 200) bending under constant pressure

Fig. 46. Column joints subjected to constant pressure and bending. (**a**) UT-type joints subjected to constant pressure and positive bending. (**b**) UT-type joints subjected to constant pressure and negative bending. (**c**) SH-RHS (120×200) bending under constant pressure. (**d**) S-RHS (120×200) bending under constant pressure.

Joint name	Axial compression ratio	M_y	M_u	K_y
UT positive bending moment	0.1 μ	36.4	57	7236
	0.2 μ	30	53.7	7109
	0.3 μ	27.3	49.7	6859
	0.4 μ	24.9	45.2	6501
	0.5 μ	18.9	38.7	6364
UT negative bending moment	0.1 μ	34.8	47.3	6304
	0.2 μ	31.6	44.1	6208
	0.3 μ	29.7	37.7	5869
	0.4 μ	24.9	29.4	5448
	0.5 μ	18.9	20.6	4833
SH 120×200	0.1 μ	51.5	79.5	13,770
	0.2 μ	37.5	63.5	10,806
	0.3 μ	18.8	42.8	8103
	0.4 μ	12.4	21.5	2505
	0.5 μ	7.45	12.1	1342
S-RHS (120×200)	0.1 μ	43.5	71.5	6702
	0.2 μ	33.5	57.5	5360
	0.3 μ	30	38	2795
	0.4 μ	15.6	18.2	1012
	0.5 μ	5.95	10.2	548

Table 8. Yield loads and initial stiffnesses of joints under balanced pressure and bending loading.

Fig. 47. UT joints with an axial compression ratio of 0.3 subjected to constant pressure and positive bending.

Fig. 48. UT joints with an axial compression ratio of 0.3 subjected to constant pressure and negative bending.
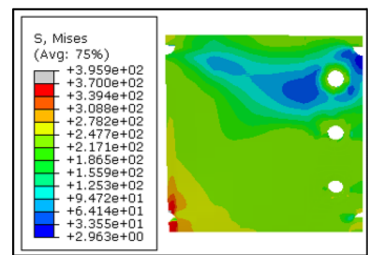
Fig. 49. SH-RHS (120×200) joint with an axial compression ratio of 0.3 and bending under constant pressure.
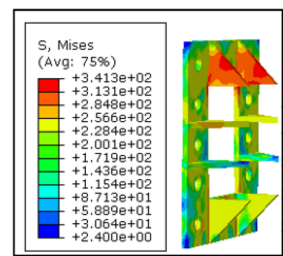

Fig. 50. S-RHS (120×200) joint with an axial compression ratio of 0.3 and bending under constant pressure.
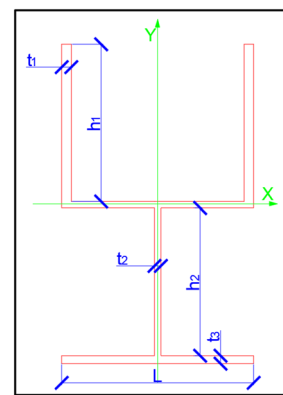

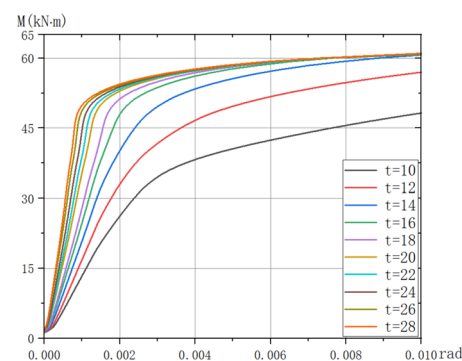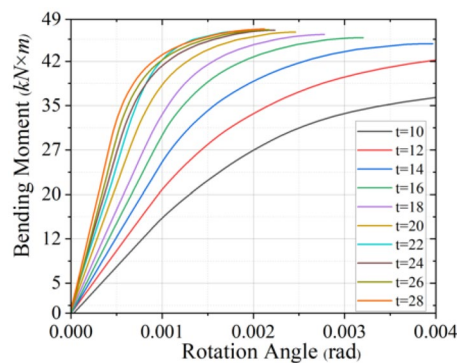**Fig. 51**. UT-type joint section.

Fig. 52. Ultimate bending moment curves for the UT-type joints with different front end plate thicknesses under positive bending moment loading.

Fig. 53. Ultimate bending moment curves for the UT-type joints with different front end plate thicknesses under negative bending moment loading.

Data availability

The authors declare that the data supporting the findings of this study are available within the paper.

References

1. Wang, J. F., Han, L. H. & Uy, B. Hysteretic behaviour of flush end plate joints to concrete-filled steel tubular columns[J]. *J. Constr. Steel Res.* **65**(8–9), 1644–1663 (2009).
2. Lu, J., Hao, J., Xue, Q. & Sun, X. Study on mechanical properties of a new type of assembled steel structure joints [J]. *Arch. Struct.* **47**(10), 39–45. https://doi.org/10.19701/J.JZJG.2017.10.008 (2017).
3. Li, Y. & Huang, B. Evaluation on seismic performance of beam-column joints of fabricated steel structure with replaceable energy-dissipating elements [J]. *Sustainability* **14**(6), 1 (2022).
4. Cao, W., & Zhang, Z. Cyclic reversed loading test of different structural beam-to-column connections in assembled steel structure [J]. *IOP Conf. Ser. Earth Environ. Sci.* **304**(5), 1 (2019).
5. Li, Y. & Huang, B. Research on load-bearing performance of new fabricated steel structure beam-column joints with energy dissipating elements[J]. *Structures* **38**, 1 (2022).
6. Liu, X. C., Zhan, X. X., Pu, S. H., Zhang, A. L. & Xu, L. Seismic performance study on slipping bolted truss-to-column connections in modularized prefabricated steel structures[J]. *Eng. Struct.* **163**, 1 (2018).
7. Liu, X. C. et al. Static and seismic experiment for welded joints in modularized prefabricated steel structure[J]. *J. Constr. Steel Res.* **112**, 1 (2015).
8. Liu, X. C. et al. Static and seismic experiment for bolted-welded joint in modularized prefabricated steel structure[J]. *J. Constr. Steel Res.* **115**, 1 (2015).
9. Wang, H., Zhao, X. & Ma, G. Experimental study on seismic performance of column-column-beam joint in panelised steel-modular structure[J]. *J. Constr. Steel Res.* **192**, 1 (2022).
10. Yan, W., Mu, T., Xie, Z. & Yu, C. Experimental investigation of typical connections for fabricated cold-formed steel structures[J]. *Adv. Struct. Eng.* **22**(1), 141 (2019).
11. Alamdari, M. M., Li, J., Samali, B., Ahmadian, H. & Naghavi, A. nonlinear joint model updating in assembled structures[J]. *J. Eng. Mech.* **140**(7), 1 (2013).
12. Yang, X., Yongfeng, L. & Qinglong, H. Research progress on seismic performance of assembled steel structures [J]. *Prog. Build. Steel Struct.* **21**(03), 1–12. https://doi.org/10.13969/j.cnki.cn31-1893.2019.03.001 (2019).
13. Lewei, T., Huang Junfeng, Yu., Peng, W. P., Jidong, Xu. & Jiachun, C. Experimental study on hysteretic behavior of staggered truss-column assembled joints [J]. *J. Tongji Univ. (Natural Science Edition)* **50**(06), 841–851 (2022).
14. Junping, Y., Yingqing, X. & Yongsheng, Z. Finite element analysis of new steel structure assembled joints [J]. *J. Guangxi Univ. Sci. Technol.* **31**(02), 25–31. https://doi.org/10.16375/j.cnki.cn45-1395/t.2020.02.004 (2020).
15. Liu Xuechun, Pu., Axin, S. X., Zhen, Ni., Ailin, Z. & Zhiwei, Y. Experimental study on static and seismic performance of modular assembled multi-storey and high-rise steel structure full-bolted joints [J]. *J. Build. Struct.* **36**(12), 43–51. https://doi.org/10.14006/J.JZJGXB.2015 (2015).
16. Gosowski, B., Lorkowski, P. & Redecki, M. Analysis of longitudinal skylights structure made of rectangular tubes in industrial hall[J]. *Thin-Walled Struct.* **108**, 234–244. https://doi.org/10.1016/j.tws.2016.08.015 (2016).
17. Guo, X. et al. Hysteretic behavior of eccentric RHS beam-to-column joints under cyclic in-plane bending [J]. *J. Constr. Steel Res.* **223**, 1 (2024).
18. Ziane, N., Ruta, G., Meftah, S. A., Doula, M. H. & Benmohammed, N. Instances of mixed buckling and post-buckling of steel RHS beams[J]. *Int. J. Mech. Sci.* **190**(1), 1 (2021).
19. Magnucki, K. & Milecki, S. Elastic buckling of a thin-walled rectangular frame under in-plane compression [J]. *Thin-Walled Struct.* **116**, 326–332 (2017).
20. Zhao, O., Gardner, L. & Young, B. Finite element modelling and design of stainless steel SHS and RHS beam-columns under moment gradients[J]. *Thin Walled Struct.* **134**, 220–232. https://doi.org/10.1016/j.tws.2018.10.004 (2019).
21. Meftah, S. A., Tounsi, A. & van Vinh, P. Formulation of two nodes finite element model for geometric nonlinear analysis of RHS beams accounting for distortion and shear deformations [J]. *Int. J. Steel Struct.* **22**(4), 940–957 (2022).
22. Zheng, L.-Q. et al. Seismic performance of prefabricated beam-to-column joint with replaceable energy-dissipating steel hinge [J]. *Bull. Earthq. Eng.* **20**(3), 1865–1895 (2022).
23. Ma, Y. C. et al. Experimental study on seismic performance of novel fabricated T-joint with replaceable steel hinges [J]. *Structures* **40**, 667–678 (2022).
24. Liu, Q. et al. Experimental study on novel energy-dissipating prefabricated beam-column joints [J]. *Adv. Civ. Eng.* **1**, 1 (2019).
25. Li, Z. H., Qi, Y. H. & Teng, J. Experimental investigation of prefabricated beam-to-column steel joints for precast concrete structures under cyclic loading [J]. *Eng. Struct.* **209**, 1 (2020).

26. Banh, T. T., Nguyen, S. H. & Lee, D. Comprehensive stress-driven multi-material problem for heat-sinking heterogeneous structures. *Compos. Struct.* **352**, 1 (2025).
27. Nguyen, M. N. & Lee, D. Design of the multiphase material structures with mass, stiffness, stress, and dynamic criteria via a modified ordered SIMP topology optimization. *Adv. Eng. Softw.* **189**, 1 (2024).
28. Banh, T. T. & Lee, D. Efficient topology optimization for geometrically nonlinear multi-material systems under design-dependent pressure loading. *Eng. Comput.* **1**, 1 (2024).
29. Banh, T. T., Lieu, Q. X., Nguyen, S. H. & Lee, D. Stress-driven design of incompressible multi-materials under frequency constraints. *Int. J. Mech. Sci.* **1**, 1 (2024).
30. Nguyen, M. N. & Lee, D. Transient heat conduction in multi-material topology optimization of thermoelastic structures involving dynamic constraints. *Compos. Struct.* **339**, 1 (2024).
31. Ministry of Housing and Urban-Rural Development of the People's Republic of China. Specification for Seismic Test of Buildings (JGJ/T 101–2015). China Architecture & Building Press, 2015.
32. Standardization Administration of China. GB/T 228.1–2021 Metallic materials—Tensile testing—Part 1: Method of test at room temperature[S]. Beijing: Standardization Administration of China, 2021.
33. Xinmin, W. *Numerical Analysis of Engineering Structures Using ANSYS[M]* (China Communications Press, 2007) (**(in Chinese)**).
34. Steel structure design standard: GB50017–2017[S]. Beijing: China Building Industry Press, 2017. (Standard for Design of Steel Structures: GB 50017–2017 [s]. Beijing: China Architecture & Building Press, 2017. (in Chinese).
35. Wei, Li. *Seismic performance study on exterior ring-plate connection of circular concrete-filled steel tubular column to steel beam frame[D]* (Tsinghua University, 2011) (**(in Chinese)**).
36. Junchao, F. *Seismic Performance Study on Prefabricated Connections of Concrete-Filled Double-Skin Steel Tubular Columns to Steel Beams[D]* (Chang'an University, 2023) (**(in Chinese)**).
37. Chen, Z. Study on Mechanical Behavior Characteristics of Steel Structure Beam-Column Connections[D]. Heilongjiang: Harbin Institute of Technology, 2022. (in Chinese).
38. Standardization Administration of China. GB/T 1229–2006 High strength large hexagon nuts for steel structures[S]. Beijing: Standardization Administration of China, 2006.
39. Architecture, C. & Press, B. *JGJ 82–2011 Technical Specification for High-Strength Bolt Connections of Steel Structures[S]* (China Architecture & Building Press, 2011) (**(in Chinese)**).
40. Beijing Times New Sky Measurement and Control Technology Co., Ltd. High-Strength Bolt Preload Reference Table[Z]. Beijing: Beijing Times New Sky Measurement and Control Technology Co., Ltd. (in Chinese).
41. Structural details of steel structure joints of multi-storey and high-rise civil buildings: 01SG519–2018[S] Beijing: China Institute of Building Standard Design, 2018.(Detailed construction of steel structure joints of multi-high-rise civil buildings: 01SG519–2018[S].Beijing: China Institute of Building Standards Design, 2017.(in Chinese).

Acknowledgements

Author contributions

S.M.H is the owner of the Research Project Fund, H.L.Y is the main writer of the research, Y.Z.L is the main theoretical provider of the research, J.X is the actual investigator of the research, and Y.M.M is the main translator of the research.

Funding

Declarations

Competing interests

The authors declare no competing interests.

Additional information

Correspondence and requests for materials should be addressed to Y.Z.

Reprints and permissions information is available at www.nature.com/reprints.

Publisher's note Springer Nature remains neutral with regard to jurisdictional claims in published maps and institutional affiliations.